Revision 1 **Word Count: 6622**

The crystal chemistry of arsenian pyrites: A Raman spectroscopic study

He Zhang[1,2], Gujie Qian[2], Yuanfeng Cai[1,*], Christopher Gibson[3,4], Allan Pring[2,*]

[1]State Key Laboratory of Mineral Deposit Research, School of Earth Sciences and Engineering, Nanjing University, Nanjing 210023, China
[2]College of Science and Engineering, Flinders University, Adelaide, SA 5042, Australia
[3]Flinders Microscopy and Microanalysis, College of Science and Engineering, Flinders University, Bedford Park, SA 5042, Australia
[4]Flinders Institute for Nanoscale Science and Technology, College of Science and Engineering, Flinders University, Bedford Park, SA 5042, Australia

ABSTRACT

A Raman spectroscopy study of the nature of the As-S substitution in natural arsenian pyrite ($Fe(S,As)_2$) is presented covering the compositional range (0.01 at% – 4.6 at% As). Three Raman-active modes were resolved in the spectrum of the nearly pure pyrite: the E_g (344 cm^{-1}), A_g (379 cm^{-1}), and $T_g(3)$ (432 cm^{-1}) modes. The Raman vibrational modes exhibit the one-mode behavior and the wavenumbers of optical modes vary continuously and approximately linearly with the As content in the arsenian pyrite, correlating with the change in bond constants with increasing substitution of As for S. The linewidth of the A_g mode was also found to increase with increasing As substitution and this is attributed to the increase in lattice strain associated with the substitution of As for S. This study provides experimental evidence for the As-induced structural evolution of pyrite from being stable to metastable before decomposing into other phases. This study illustrates that a

systematic Raman spectroscopic investigation of the crystal chemistry of arsenian pyrite enables us to further understand this process of the structural strain associated with elemental substitution. The results of this study and the results of another recent Raman study of arsenian pyrite where As substitution has a more complex form indicates that it is not possible to use the shift in the Raman bands to establish the As content, but rather for a given As content it is possible to establish the nature of the As substitution, As for S or As for Fe or both.

Keywords: arsenian pyrites, Raman spectroscopy, solid solution, lattice defects

INTRODUCTION

Arsenian pyrite ($Fe(S,As)_2$) is defined as pyrite containing anywhere from several ppm to ~19 wt% arsenic (e.g., Abraitis et al., 2004; Qian et al., 2013; Reich and Becker, 2006) and this substitution is commonly associated with the presence of economically important metals such as Au, Co, Ni, Ag, Cu etc (Deditius et al., 2014; Large et al., 2014; Reich et al., 2005, 2013). Understanding the crystal chemistry of arsenian pyrite can help design strategies to control the release of toxic metal(loid)s, explore the enrichment mechanism of valuable metals, and optimize the methods of mining and smelting of sulfide/pyritic ores. These factors have motivated the study of the crystal chemistry of arsenian pyrite over the last three decades (e.g., Abraitis et al., 2004; Cook and Chryssoulis, 1990; Deditius et al., 2008, 2011; Deditius and Reich 2016; Filimonova et al., 2020; Fleet et al., 1993; Merkulova et al., 2019; Reich et al., 2005; Reich and Becker, 2006; Simon et al., 1999a, b). Central to this issue is the nature of As incorporation and its effect on the pyrite structure. The pyrite structure is

derived from the NaCl structure with Fe in the Na position in a face centered array while the Cl ion position is replaced by the disulfide ion, with the orientation of the S–S bond aligned with the body diagonal of the cell, but such that the symmetry is lower from *Fm*3*m* to *Pa*3 (Fig. 1). This results in FeS_6 octahedra with the corners linked by the S_2^{2-} ions. Each S is bonded to 3 Fe ions and a S in a tetrahedral arrangement. The Fe–S and S–S bond lengths are 2.262 Å and 2.177 Å, respectively (Brostigen and Kjekshus 1969, Vaughan and Craig 1978). Five Raman active modes ($A_g + E_g + 3T_g$) are predicated for pyrite based on a group theory analysis of the lattice vibrations, with these modes involving only the movements of the S ions (Mernagh and Trudu, 1993; Sourisseau et al., 1991; Vogt et al., 1983). Arsenic can substitute for S in the disulfide ion or Fe in the octahedral site. Fe-S-As (at%) ternary diagram can be used to identify the nature of substitutions of As for either Fe or S for a series of compositional data from a sample; with As^{3+}-pyrite and As^{1-}-pyrite trends being parallel to the As-Fe and As-S joins, respectively (Deditius et al., 2008; Liang et al., 2013) (Fig. 2).

A suite of experimental studies, that include secondary ionization mass spectrometry (SIMS), electron microprobe analyzer (EMPA), X-ray photoelectron spectroscopy (XPS), X-ray absorption near-edge structure (XANES) and extended X-ray absorption fine structure (EXAFS), have confirmed that As^{1-} substitutes for S^{1-} in the disulfide ion (S_2^{2-}) as AsS^{2-} pairs (e.g., Cook and Chryssoulis, 1990; Deditius et al., 2008; Fleet and Mumin, 1993; Fleet et al., 1997; Manceau et al., 2020; Reich et al., 2005; Savage et al., 2000; Simon et al., 1999a). In contrast, a few studies have

indicated that As can also substitute Fe in pyrite as either As^{3+} (Deditius et al., 2008) based on the XPS analysis, or As^{2+} (Qian et al., 2013) based on the XPS and XANES analyses. The different valence states of As in arsenian pyrite have been linked to the physiochemical conditions of pyrite formation, with oxidizing and reducing conditions forming As^{3+}-pyrite and As^{1-}-pyrite, respectively (Deditius et al., 2008; Kesler et al., 2011). In addition, arsenic is identified as clusters (As^0) in amorphous Fe-As-S nanoparticles (~50 nm in diameter) in pyrite (Deditius et al., 2009).

The anionic As^{1-} substitution into pyrite causes the breaking of S–S bonds and hence point defects in pyrite (Fleet and Mumin, 1997). An expansion of the unit cell of As^{1-}-pyrite relative to end member pyrite has been identified based on the EXAFS data (Manceau et al., 2020; Savage et al., 2000). Such defects are expected to facilitate and accommodate larger-size ions (e.g., Au) within the structure. The positive As-dependence of Au in As^{1-}-pyrite is closely related to the As-induced defects (Arehart et al., 1993; Fleet et al., 1993; Gopon et al., 2019; Morishita et al., 2018; Reich et al., 2005) and recently interpreted as a possible signature for an atomic-scale $AuAs_6$ coordination (Merkulova et al., 2019). Additionally, local highly defective regions could be produced by As-induced lattice strain. Stacking faults (~10–12 Å wide) are observed within As^{1-}-pyrite and reflect the presence of unit-cell scale lamellae of marcasite (FeS_2) and/or arsenopyrite (FeAsS) (Cabri et al., 1989; Dodony et al., 1996; Fleet et al., 1989; Simon et al., 1999a). Atomistic calculations indicate energetically favored tendency of As to form arsenopyrite-type clusters in As^{1-}-pyrite (Manceau et al., 2020). Such marcasite-like interlayers were not observed

in As^{1-}-pyrite in some other reports (e.g., Palenik et al., 2004; Savage et al., 2000), but two types of nanostructures were observed in As^{1-}-pyrite, with one polycrystalline matrix consisting of Fe-sulfides (arsenian pyrite and arsenopyrite/pyrrhotite), and the other highly crystalline matrices of pure arsenian pyrite (Palenik et al., 2004).

Despite the numerous studies undertaken into the nature of As substitution in pyrite, little is known about the As-induced variations in the pyrite structure. The positions and widths of the optical band gap are highly sensitive to structural evolution (e.g., Eyert et al., 1998; Yang et al., 1994) yet the only Raman spectroscopic study of As substitution in pyrite has only recently been published by Zhu et al. (2020). They studied arsenian pyrites from the Shizilishan Sr-(Pb-Zn) deposit in eastern China and found a significant correlation between an increase in As content and a downward shift of the position of the Raman bands for As substitution increased to up to 4.89 wt% (Zhu et al. 2020). The present work reports on the Raman active modes of As-pyrite and presents evidence for the As-induced structural variations in pyrite associated with the substitution of As for S in pyrite.

MATERIALS AND METHODS

Materials

Ore samples were collected from the Dongyang epithermal gold deposit that is in the Dehua prospecting region of central Fujian Province, southeast China. This deposit is a typical low sulfidation epithermal deposit, with characteristics of mineralization previously reported (Li et al., 2018; Xu et al., 2018, 2019; Zhang et al.,

116 2018). It should be noted that the conditions (e.g., temperature and pressure) of
117 arsenian pyrite crystallization might cause variations in crystal chemistry of the
118 mineral. Thus, this study mainly focuses on arsenian pyrites from the thin-section of
119 sample DY1033-10 which was previously characterized in detail by Zhang et al (2018;
120 2020). The samples used in the current study were in the form of 100-μm-thick
121 polished thin sections (Fig. 3). The pyrite grains were in the size range of 50 –500 μm.
122

123 **Electron microprobe analysis**

124 The chemical compositions of arsenian pyrite were determined using electron
125 microprobe analysis (EMPA) employing a Cameca CAMEBAX SX51 instrument at
126 Adelaide Microscopy, University of Adelaide. Prior to analysis, the thin-sections were
127 re-polished, cleaned in ethanol to remove any oxide layers and impurities from the
128 sample surface. The analytical points were chosen based on the series of the
129 backscattered electron (BSE) images of arsenian pyrites ("brighter" contrast
130 corresponding to higher As; Fig. 3). The analyses were undertaken using an
131 accelerating voltage of 20 kV, a beam current of 20 nA, and a spot size of the electron
132 beam of 1 μm in diameter. Elements, X-ray lines and standards used were: Fe
133 *Kα*/chalcopyrite, S *Kα*/chalcopyrite, As *Lα*/gallium arsenide (Astimex Standards Ltd.),
134 Co *Kα*/pyrite, Ni *Kα*/ nickel, Sb *Lα*/stibnite (Astimex), Ag *Lα*/silver. The degree of As
135 substitution was calculated in terms of at% based on Fe + S + As = 3 rather than
136 assuming a simple binary As for S solid solution.
137

Electron backscatter diffraction analysis

Crystallographic orientation data of pyrite were collected by indexing electron backscatter diffraction (EBSD) Kikuchi patterns using the SEM-EBSD facility at the State Key Laboratory for Mineral Deposition Research, Nanjing University, China. The diffraction patterns were generated by the interaction of a vertical incident electron beam with a highly polished thin section tilted at 70° in high vacuum mode by using a scanning electron microscope (JEOL JSM-6490). The analyses were operated at 20 kV and 17-25 mm working distance.

Laser Raman analysis

Raman spectra were measured on the polished thin sections of arsenian pyrite using a Witec alpha300R Raman microscope at an excitation laser wavelength of 532 nm using a 100x objective (numerical aperture 0.90) at Flinders University given a beam diameter of around 500 nm. Typical integration times for single Raman spectrum were 30 s for 2-3 accumulations. The highest resolution grating available on the instrument was used which is 1800 grooves mm^{-1} and gave a spectral resolution of ~1 cm^{-1}. Laser power levels were kept as low as possible to prevent sample damage with the power equal to approximately 1.5 mW. Laser power was kept constant during measurements. A recent article by Bryant et al., (2018) demonstrated that for a pyrite grain size ~ 1 μm then a laser power ~0.8 mW should avoid or reduce heating effects while for a pyrite grain size ~100 μm then up to 2.6 mW could be used without adverse heating effects. Zhu et al., (2020) observed that for their samples, which had

grain sizes greater than 100 μm, 3.5 mW could be used without significant heating effects. The effect of laser power was further investigated on two of our samples (one with ~3.8 at% As and the other ~0.4 at% As) using a Renishaw RW2000 laser Raman microscope at an excitation wavelength of 514 nm using a 50x objective (numerical aperture 0.75) at Nanjing University. Typical integration times for single Raman spectrum were 30 s for 2 accumulations. The highest resolution grating available on the instrument was used which is 1800 grooves mm^{-1}. It was found that laser induced heating effect was not significant below 4.5 mW (Fig. S1). This data in combination with the observations of Bryant et al. (2018) and Zhu et al. (2020) and the grain size of our samples (50 to 500 μm) indicates our estimated laser power will not cause significant laser heating of the sample surface. All spectral measurements reported in this work were fitted using combined Gaussian/Lorentzian amplitude functions using PeakFit (version 4.12).

RESULTS

Chemistry of arsenian pyrite

The samples were examined by reflected light microscopy, where the arsenian pyrite occurs as light brass-yellow subhedral and anhedral grains or aggregates with no obvious inclusions of other sulfides. Figure 3 shows arsenic-rich pyrites (Py1) overgrown by As-deficient pyrite aggregates (Py2), with their chemical compositions given in Table S1. Arsenic concentrations range from effectively zero (0.01 at%) to 4.55 at%. The compositions fall close to the FeS_2-FeAsS join as the concentrations of

most other impurity elements are at least one order of magnitude lower than the As concentrations. The antimony levels should, however, be noted with some anomalies (e.g., 0.49 at% in the sample DY1033-10-2), which also probably has an effect on the pyrite structure by isomorphic substitution.

Arsenic substitution in arsenian pyrite

Fe-S-As (at%) ternary diagram is used to identify the nature of substitutions of As for either Fe or S, with As^{3+}-pyrite and As^{1-}-pyrite trends being parallel to the As-Fe and As-S joins, respectively (Deditius et al., 2008; Liang et al., 2013). Our data shows a dispersed trend approximately parallel to the As-S join (arrow 1) in this diagram (Fig. 2), consistent with the As^{1-} substitution for S^{1-} within the structure. The deviation from the arrow 1, that indicates ideal one-for-one substitution, might be caused by the substitution of other trace elements (e.g., Sb) or vacancies in the Fe and S sites (Deditius et al., 2008). A notable negative correlation ($R^2 = 0.98$) in this binary diagram (Fig. 2b) does confirm that the substitution takes the form of As^{1-} for S^{1-} in the disulfide ion, but a poor negative correlation for As for Fe (($R^2 = 0.38$) (Fig. 2c)). The compositional data of Zhu et al., (2020) is also plotted on Fig 2 and shows that in their samples the As substitutes both for Fe and S. This is highlighted in Figures 2b and c, which shows a strong correlation of As for Fe ($R^2 = 0.90$) and As for S ($R^2 = 0.95$).

Raman scattering spectra

Previous studies have reported five Raman-active modes in pyrite (Sourisseau et al., 1991; Vogt et al., 1983), a doubly degenerate mode (E_g, 343 cm^{-1}), three triply degenerate modes ($T_g(1)$, 350 cm^{-1}; $T_g(2)$, 377 cm^{-1}; $T_g(3)$, 430 cm^{-1}), and a totally symmetric mode (A_g, 379 cm^{-1}). The E_g vibrational mode is attributed to displacements of S^{-} ions perpendicular to the S–S bond axis. The A_g and $T_g(2)$ modes represents in-phase and out-of-phase S–S stretching vibrations, respectively. Tg(1) and $T_g(3)$ correspond to a combination of vibrational and stretch motions (Sourisseau et al., 1991). Of these, only three vibrational modes (E_g, A_g and $T_g(3)$) have been reported to be easily observed with the sequence of band energies commonly defined as $\nu(A_g) > \nu(E_g) > \nu(T_g)$ (Anastassakis and Perry, 1976; Bryant et al., 2018; Kleppe and Jephcoat, 2004; Mernagh and Trudu, 1993; Ushioda, 1972; Zhu et al., 2020). It is difficult to resolve the A_g and $T_g(2)$ modes due to their frequencies being only ≤ 2 cm^{-1} apart and the A_g mode has a stronger intensity than the $T_g(2)$ mode and dominates the spectrum (Kleppe and Jephcoat, 2004). The $T_g(1)$ mode is also difficult to be observed due to its low intensity, and is only distinguishable under compression (Kleppe and Jephcoat, 2004).

The ambient Raman vibrational spectra of the natural As-pyrites (arsenic concentrations of 0.4–4.6 at%) were recorded over the 500 cm^{-1} and 250 cm^{-1} spectral range in this study. Representative Raman spectra of the As-pyrite samples are shown in Figure 4. Three Raman bands are observed in this spectrum at 344, 379, and 432 cm^{-1} for 0.4 at% As sample (Fig. 4b). These bands are in good agreement with the previously published data and assigned to the S_2 vibration in the E_g mode, the S–S

226 in-phase stretching in the A_g mode, and the coupled vibration and stretch in the $T_g(3)$
227 mode, respectively (Kleppe and Jephcoat, 2004; Mernagh and Trudu, 1993; Vogt et al.,
228 1983). In comparison, three Raman bands at 331, 363, and 414 cm^{-1} for 4.6 at% As
229 samples (Fig. 4a) should be assigned to E_g, A_g and $T_g(3)$ modes, respectively. The
230 shifts in the Raman spectra with the increasing As concentration are shown in Figure
231 5, including (1) Raman band positions shifting to the lower wavenumbers; (2) Raman
232 band broadening; (3) the E_g and $T_g(3)$ modes gradually weakening with increasing As
233 substitution.

234 The Raman band positions, intensities, and the full widths at half maximum
235 (FWHMs) for As-pyrite samples are summarized in Table S2. Figure 6 shows that the
236 Raman band wavenumbers and FWHMs plotted against the atomic fraction of As.
237 The strikingly inverse correlation between As-content and the wavenumbers of the E_g,
238 A_g and $T_g(3)$ modes of As-pyrite confirms the As-induced redshift of the Raman
239 bands (Fig. 6a-c), with the maximum offset values of approximately 25 cm^{-1}, 27.5
240 cm^{-1} and 30 cm^{-1} for the three Raman modes, respectively. The effect of the minor
241 substitution of antimony should also be considered, since it produces some anomalies
242 in the data with Sb outliers highlighted in red in Figure 6. The distinct influence of Sb
243 substitution on the correlation between position of the Raman bands and As content in
244 pyrite is, however, negligible. The deviation from an ideal correlation (Fig. 6a-c), that
245 would represent an ideal one-for-one shift, possibly results from additional trace
246 elements in the pyrite or vacancies in the Fe and S sites. The uneven As distribution at
247 the μm-scale may also be linked to deviation from an ideal correlation.

The FWHMs of the Raman active modes is weakly dependent on the As content: the A_g mode shows some indication of positive correlation but those of the E_g and $T_g(3)$ modes seem random (Fig. 6d-f). The FWHMs of the E_g, A_g and $T_g(3)$ modes increase from approximately 9.5 cm^{-1}, 12.6 cm^{-1}, and 14 cm^{-1} at 0.4 at% As, to 18.5 cm^{-1}, 29 cm^{-1}, and 33.8 cm^{-1} at 4.6 at% As, respectively, but the scatter of values is high. With the As content increase a splitting of these Raman bands into possible impurity modes cannot be excluded. However, it should be noted that the Raman spectra are characterized by symmetric bands and absence of obvious new impurity-induced bands.

The intensity ratio of A_g mode relative to E_g mode is moderately dependent on the As content (Fig. 7). Band intensity ratios in Raman spectra for pyrite are recently reported to markedly depend on the unit cell orientation with respect to the plane of polarization of the laser (Bryant et al., 2018). EBSD data were acquired for some of those pyrite grains analyzed by Raman in this study (Table S3). The results of the orientational dependence is illustrated by the Raman spectra for two pyrite grains with ~ 3.7 at% As but with a difference in orientation of 21° (Fig. 8b) and one exhibits markedly stronger intensities of A_g and E_g modes but a lower intensity ratio, but there is no shift in the position of the bands. Another crystal with 1.5 at% As, with an rotation angle 6° (Fig. 8c) has weaker intensities and intensity ratio of A_g and E_g modes. In comparison, the spectra for two grains – that contain the same As content with minor orientational difference (4°) – show nearly identical intensity of A_g mode, but different intensities of E_g and intensity ratio of A_g relative to E_g (Fig. 8d). These

results suggest a combined effect of crystal orientation and As contents on the band intensity in pyrite Raman spectra, but that orientational differences do not affect the band positions.

DISCUSSION

Interpretation of Raman spectra

Based on "harmonic oscillator model" and Hooke's law, the wavenumber of Raman vibrational modes can be shifted with the isomorphic substitution of one element for another, towards lower wavenumbers with decrease of bond strength and increase of atomic mass (e.g., Kharbish et al., 2007). The As-induced shifts of the Raman vibrational modes of pyrite are attributed to the greater atomic mass of As (74.92) than S (32.01), which results in the lower wavenumbers of the Raman bands (Figs. 5 and 6), and also affected by the bond strength that is closely related to the valence, electronegativity, coordination number and, most notably, bond length between atoms or ions (Eyert et al., 1998; Gordy, 1946). In the case of pyrite, the stretching vibration (A_g) is strongly controlled by the S–S force constant (Lutz and Zwinscher, 1996); while the vibrational mode (E_g), and coupled vibrational and stretching mode ($T_g(3)$) are controlled by the Fe–S force constant (Lutz and Zwinscher, 1996; Sourisseau et al., 1991). Kleppe and Jephcoat (2004) attributed a pressure-induced blueshift of the Raman vibrational modes of pyrite to a shortening of the Fe–S and S–S bonds under compression. Pačev ki et al. (2008) attributed a redshift of the Raman modes of Cu-bearing pyrite to an elongating and weakening of bonds caused by substitution of Fe by Cu. Arsenic substitution into pyrite induces an

292 expansion of the unit-cell (Blanchard et al., 2007; Manceau et al., 2020; Savage et al.,
293 2000), the dimension of which is proportional to the As concentration, as As–S and
294 As–Fe bonds are approximately 4.6% and 2.8% longer than S–S and Fe–S bonds,
295 respectively (see Introduction) (Blanchard et al., 2007). Thus, the substitution of As
296 for S changes the Fe–S and S–S bond constants, and hence causes the redshifts of
297 Raman vibrational modes observed in this study. Similar phenomenon has been
298 recently reported by Zhu et al. (2020), with possible effect of other factors (e.g., laser
299 powers and polishing) also discussed on pyrite Raman band positions. The redshift
300 they observed were significantly lower than those we found, (~10 cm^{-1} vs ~20 cm^{-1}
301 for similar levels of As substitutions (~3 at%). The compositional data from Zhu et al.
302 (2020) is included in Figure 2 and show strong correlations for As replacing S, and As
303 replacing Fe in the octahedral sites and it appears that the two modes of As
304 substitution can occur simultaneously on a submicron scale, given the 1 μm laser
305 beam diameter in the Raman system.

306 The As–S substitution may cause local strains and structural variations in pyrite
307 (e.g., Fleet and Mumin, 1997; Gopon et al., 2019). The crystal quality is expected to
308 be reflected in line-shapes of Raman spectra, with the shifting and broadening Raman
309 bands of amorphous material relative to the well-crystalline bulk (Kumar et al., 2010,
310 2014; Smith et al., 1971; Temple and Hathaway, 1973). Yang et al. (1994) investigated
311 porous silicon and found that built-in lattice strain causes Raman redshift and line
312 broadening. Pring et al. (2008) identified a slight line broadening of the infrared
313 absorption bands for Fe-doped sphalerite and attributed it to the minor structural

distortions due to Fe^{2+} substitution for Zn^{2+}, due to a small discrepancy between Fe–S (2.357 Å) and Zn–S (2.345 Å) bond lengths. As such, the remarkable line broadening (Fig. 5) most likely reflects strain associated with As^{1-} in pyrite. The difference of atomic size between S (1.03 Å) and As (1.20 Å; Manceau et al., 2020) also supports the generation of strain associated with the substitution of As^{1-} for S^{1-} in the pyrite structure.

Arsenic-induced structural evolution of pyrite

Ternary compounds are classified into two major classes on the basis of the behavior of optical phonons (e.g., Chang and Mitra, 1968; Kang et al., 2009; Pring et al., 2008; Peterson et al., 1986; Stingl et al., 1992), including (1) the one-mode behavior that optical mode wavenumbers vary continuously and approximately linearly with the concentration between the wavenumbers of the two end-members; (2) the two-mode behavior that two sets of optical phonon modes occur at wavenumbers close to two pure end-members, with the intensity of each mode approximately proportional to the concentration between the wavenumbers of the two end-members. The premise behind the discussion above is that the two end-members should have the same structure and similar force constants for a given mixed ternary crystals (e.g., Pring et al., 2008). However, arsenic is commonly incorporated into pyrite as a trace or minor element with a restricted solubility (e.g., Abraitis et al., 2004). A continuous solid-solution series from pyrite (FeS_2; *Pa3*), through arsenopyrite (FeAsS; $P2_1/c$), to löllingite ($FeAs_2$; *Pnnm*) is not observed in nature due to their different structural

336 topologies. Hence, our study only investigates arsenian pyrites with the As content up
337 to 4.6 at% (8.2 wt%). The continuous redshifts with the increasing As content are
338 presented for all Raman bands (Figs. 5 and 6), and no impurity-induced Raman bands
339 occur, and this corresponds to the one-mode behavior. If that is the case, one would
340 expect that the As–S substitution would not cause the pyrite structure to transform to a
341 new structure or separate into two separate phases, as consistent with the maximum
342 solubility of As (~5 at%; Reich and Becker, 2006). Above the maximum As solubility,
343 for the As for S substitution, fine scale intergrowth of arsenopyrite or marcasite-like
344 lamellae (~10–12 Å) occur (e.g., Dodony et al., 1996; Fleet et al., 1989; Simon et al.,
345 1999a). Furthermore, the lower sulfur fugacity in hydrothermal systems not only
346 facilitates increasing substitution of As for S in pyrite (Spycher and Reed, 1989; Reich
347 et al., 2005), but also stabilizes the marcasite form of FeS_2 over pyrite form, as
348 marcasite is slightly S-deficient and thermodynamically stable at lower sulfur fugacity
349 than pyrite (Buerger, 1934).

350 Additionally, calculations by Manceau et al. (2020) indicate the lowest energy
351 bonding environment of As in pyrite is similar to local structure of As in arsenopyrite.
352 Blanchard et al. (2007) predicted that AsS^{2-} unit is energetically more favored than
353 the $AsAs^{2-}$ by density functional theory (DFT) calculations. Are the As-induced
354 Raman features perhaps indicative of some clustering of As atoms in the pyrite
355 structure? Here Fe-bearing sphalerite (Fe,Zn)S is taken as a comparison with
356 As-bearing pyrite. Fe^{2+}–Fe^{2+} pairs and Fe^{2+} clusters were identified in the Fe-bearing
357 sphalerite ((Fe,Zn)S; Balabin and Sack, 2000; Di Benedetto et al., 2005; Twardowski

et al., 1988), which is reflected by non-monotonic behavior of Raman intensities with increasing Fe substitution for Zn (Osadchii and Gorbaty, 2010). In the case of As^{1-}-pyrite, both the Raman band positions and FMHWs appear to vary in a continuous and linear manner upon As-S exchange, indicating the absence of As^{1-}–As^{1-} clusters in the pyrite structure. In conclusion, the linear behavior of As-induced band redshifts and line broadening should reflect the structural evolution of pyrite from being stable to metastable before decomposing into marcasite and/or arsenopyrite.

IMPLICATIONS

In this contribution, the innovative use of Raman spectroscopy has captured pyrite structural variations associated with As-S substitution. As-induced lattice defects and strains within pyrite are potentially crucial in enhancing the capacity of arsenian pyrite to incorporate valuable metal ions with large effective ionic radii. The As-induced lattice defects are also inferred to play an important role in accelerating the weathering of arsenian pyrite and thus releasing of toxic heavy ions into the environment, with previous study reporting faster oxidation, hydrolysis, and dissolution of arsenian pyrite than pure pyrite (e.g., Savage et al., 2000). This study provides experimental evidence for the As-induced structural evolution of pyrite before decomposing into other mineral phases. Such information is of significance in understanding the mechanisms of isomorphic substitution in solid solution series. Generally, the further application of Raman spectroscopy has the potential to intuitively clarify the effects of elemental substitution on the crystal structure. Our

results and those of Zhu et al (2020) show that it is not possible to simply use the size of the Raman redshift on the arsenian pyrite spectra to simply determine the As composition, as the nature of the substitution mechanism has a major effect on redshift. Rather it should be possible from the redshift and compositional data to establish the nature of the substitution As for S or As for Fe.

ACKNOWLEDGEMENTS

We thank Benjamin Wade for his assistance with EMPA, Juan Li for assistance with EBSD, and Junying Ding for assistance with laser Raman. This paper greatly benefited from constructive comments and thorough reviews from Ray Frost, Wei Tan and two anonymous referees. This study was financially supported by the Australian Research Council (Grants DP140102765, DP200102248), the NSFC projects (Grants 41830426 and 41272055), National Key R&D Program of China (Grant 2016YFC0600205), the China Geological Survey (Grant 12120115034601), and joint Ph.D. project funding from the China Scholarship Council (Grant 201806190162). The authors also acknowledge the expertise, equipment and support provided by Microscopy Australia at the South Australian nodes under the National Collaborative Research Infrastructure Strategy.

REFERENCES CITED

Abraitis, P.K., Pattrick, R.A.D., and Vaughan, D.J. (2004) Variations in the compositional, textural and electrical properties of natural pyrite: a review.

International Journal of Mineral Processing, 74, 41–59.

Anastassakis, E. and Perry, C.H. (1976) Light scattering and ir measurements in XS_2 pryite-type compounds. The Journal of Chemical Physics, 64, 3604–3609.

Arehart, G.B., Chryssoulis, S.L., and Kesler, S.E. (1993) Gold and arsenic in iron sulfides from sediment-hosted disseminated gold deposits: Implications for depositional processes. Economic Geology, 88, 171–185.

Balabin, A.I., and Sack, R.O. (2000) Thermodynamics of (Zn,Fe)S sphalerite. A CVM approach with large basis clusters. Mineralogical Magazine, 64, 923–943.

Blanchard, M., Alfredsson, M., Brodholt, J., Wright, K., and Catlow, C.R.A. (2007) Arsenic incorporation into FeS_2 pyrite and its influence on dissolution: a DFT study. Geochimica et Cosmochimica Acta, 71, 624–630.

Brostigen, G. and Kjekshus, A. (1969) Redetermined crystal structure of FeS_2 (Pyrite). Acta Chemica Scandinavica, 23, 2186–2188.

Bryant, R.N., Pasteris, J.D., and Fike, D.A. (2018). Variability in the Raman spectrum of unpolished growth and fracture surfaces of pyrite due to laser heating and crystal orientation. Applied Spectroscopy, 72, 37–47.

Buerger, M.J. (1934) The pyrite–marcasite relation. American Mineralogist, 19, 37–61.

Cabri, L.J., Chryssoulis, S.L., de Villiers, J.P., Laflamme, J.G., and Buseck, P.R. (1989) The nature of "invisible" gold in arsenopyrite. The Canadian Mineralogist, 27, 353–362

Chang, I.F. and Mitra, S.S. (1968) Application of a modified

424 random-element-isodisplacement model to long-wavelength optic phonons of mixed
425 crystals. Physical Review, 172, 924–933.
426 Cook, N.J. and Chryssoulis, S.L. (1990) Concentrations of invisible gold in the
427 common sulfides. The Canadian Mineralogist, 28, 1–16.
428 Deditius, A.P. and Reich, M. (2016) Constraints on the solid solubility of Hg, Tl, and
429 Cd in arsenian pyrite. American Mineralogist, 101, 1451–1459.
430 Deditius, A.P., Reich, M., Kesler, S.E., Utsunomiya, S., Chryssoulis, S.L., Walshe, J.,
431 and Ewing, R.C. (2014) The coupled geochemistry of Au and As in pyrite from
432 hydrothermal ore deposits. Geochimica et Cosmochimica Acta, 140, 644–670.
433 Deditius, A.P., Utsunomiya, S., Ewing, R.C., and Kesler, S.E. (2009) Nanoscale
434 "liquid" inclusions of As-Fe-S in arsenian pyrite. American Mineralogist, 94, 391–
435 394.
436 Deditius, A.P., Utsunomiya, S., Reich, M., Kesler, S.E., Ewing, R.C., Hough, R., and
437 Walshe, J. (2011) Trace metal nanoparticles in pyrite. Ore Geology Reviews, 42, 32–
438 46.
439 Deditius, A.P., Utsunomiya, S., Renock, D., Ewing, R.C., Ramana, C.V., Becker, U.,
440 and Kesler, S.E. (2008) A proposed new type of arsenian pyrite: Composition,
441 nanostructure and geological significance. Geochimica et Cosmochimica Acta, 72,
442 2919–2933.
443 Di Benedetto, F., Andreozzi, G.B., Bernardini, G.P., Borgheresi, M., Caneschi, A.,
444 Cipriani, C., Gatteschi, D., and Romanelli, M. (2005) Short-range order of Fe^{2+} in
445 sphalerite by ^{57}Fe Mössbauer spectroscopy and magnetic susceptibility. Physics and

446 Chemistry of Minerals, 32, 339–348.

447 Dodony, I., Pósfai, M., and Buseck, A.R. (1996) Structural relationship between pyrite
448 and marcasite. American Mineralogist, 81, 119–125.

449 Eyert, V., Höck, K.H., Fiechter, S., and Tributsch, H. (1998) Electronic structure of
450 FeS_2: The crucial role of electron-lattice interaction. Physical Review B, 57, 6350–
451 6359.

452 Filimonova, O.N., Tagirov, B.R., Trigub, A.L., Nickolsky, M.S., Rovezzi, M.,
453 Belogub, E.V., Reukov, V.L., and Vikentyev, I.V. (2020) The state of Au and As in
454 pyrite studied by X-ray absorption spectroscopy of natural minerals and synthetic
455 phases. Ore Geology Reviews, 121, 103475.

456 Fleet, M.E., Chryssoulis, S.L., MacLean, P.J., Davidson, R., and Weisener, C.G. (1993)
457 Arsenian pyrite from gold deposits: Au and As distribution investigated by SIMS and
458 EMP, and color staining and surface oxidation by XPS and LIMS. The Canadian
459 Mineralogist, 31, 1–17.

460 Fleet, M.E., MacLean, P.J., and Barbier, J. (1989) Oscillatory-zoned As-bearing
461 pyrite from strata-bound and stratiform gold deposits: an indicator of ore fluid
462 evolution. Economic Geology Monograph 6, 356–362.

463 Fleet, M.E. and Mumin, A.H. (1997) Gold-bearing arsenian pyrite and marcasite and
464 arsenopyrite from Carlin Trend gold deposits and laboratory synthesis. American
465 Mineralogist, 82, 182–193.

466 Gopon, P., Douglas, J.O., Auger, M.A., Hansen, L., Wade, J., Cline, J.S., Robb, L.J.,
467 and Moody, M.P. (2019) A Nanoscale Investigation of Carlin-Type Gold Deposits: An

468 Atom-Scale Elemental and Isotopic Perspective. Economic Geology, 114, 1123–1133.

469 Gordy, W. (1946) A relation between bond force constants, bond orders, bond lengths,

470 and the electronegativities of the bonded atoms. The Journal of Chemical Physics, 14,

471 305–320.

472 Kang, T.T., Hashimoto, A., and Yamamoto, A. (2009) Raman scattering of

473 indium-rich $Al_xIn_{1-x}N$: Unexpected two-mode behavior of A_1 (LO). Physical Review

474 B, 79, 033301.

475 Kesler, S.E., Deditius, A.P., Reich, M., Utsunomiya, S., and Ewing, R.C. (2011) Role

476 of arsenian pyrite in hydrothermal ore deposits: a history and update. Geological

477 Society of Nevada Symposium, May 14–22.

478 Kharbish, S., Libowitzky, E., and Beran, A. (2007) The effect of As–Sb substitution in

479 the Raman spectra of tetrahedrite–tennantite and pyrargyrite–proustite solid solutions.

480 European Journal of Mineralogy, 19, 567–574.

481 Kleppe, A.K. and Jephcoat, A.P. (2004) High-pressure Raman spectroscopic studies of

482 FeS_2 pyrite. Mineralogical Magazine, 68, 433–441.

483 Kumar, R., Mavi, H.S., and Shukla, A.K. (2010) Spectroscopic investigation of

484 quantum confinement effects in ion implanted silicon-on-sapphire films. Silicon, 2,

485 25–31.

486 Kumar, R., Sahu, G., Saxena, S.K., Rai, H.M., and Sagdeo, P.R. (2014) Qualitative

487 evolution of asymmetric Raman line-shape for nanostructures. Silicon, 6, 117–121.

488 Large, R.R., Halpin, J.A., Danyushevsky, L.V., Maslennikov, V.V., Bull, S.W., Long,

489 J.A., Gregory, D.D., Lounejeva, E., Lyons, T.W., and Sack, P.J. (2014) Trace element

content of sedimentary pyrite as a new proxy for deep-time ocean–atmosphere evolution. Earth and Planetary Science Letters, 389, 209–220.

Li, S.N., Ni, P., Bao, T., Li, C.Z., Xiang, H.L., Wang, G.G., Huang, B., Chi, Z., Dai, B.Z., and Ding, J.Y. (2018) Geology, fluid inclusion, and stable isotope systematics of the Dongyang epithermal gold deposit, Fujian Province, southeast China: Implications for ore genesis and mineral exploration. Journal of Geochemical Exploration, 195, 16–30

Liang, J.L., Sun, W.D., Li, Y.L., Zhu, S.Y., Li, H., Liu, Y.L., and Zhai, W. (2013) An XPS study on the valence states of arsenic in arsenian pyrite: implications for Au deposition mechanism of the Yang-shan Carlin-type gold deposit, western Qinling belt. Journal of Asian Earth Sciences, 62, 363–372.

Lutz, H.D., and Zwinscher, J. (1996) Lattice dynamics of pyrite FeS_2–polarizable–ion model. Physics and Chemistry of Minerals, 23, 497–502.

Manceau, A., Merkulova, M., Mathon, O., Glatzel, P., Murdzek, M., Batanova, V., Simionovici, A., Steinmann, S.N., and Paktunc, D. (2020) The mode of incorporation of As (-I) and Se (-I) in natural pyrite revisited. ACS Earth and Space Chemistry, 4, 379–390.

Merkulova, M., Mathon, O., Glatzel, P., Rovezzi, M., Batanova, V., Marion, P., Boiron, M.C., and Manceau, A. (2019) Revealing the chemical form of “invisible” gold in natural arsenian pyrite and arsenopyrite with high energy-resolution X-ray absorption spectroscopy. ACS Earth and Space Chemistry, 3, 1905–1914.

Mernagh, T.P. and Trudu, A.G. (1993) A laser Raman microprobe study of some

512 geologically important sulphide minerals. Chemical Geology, 103, 113–127.

513 Morishita, Y., Shimada, N., and Shimada, K. (2018) Invisible gold in arsenian pyrite
514 from the high-grade Hishikari gold deposit, Japan: Significance of variation and
515 distribution of Au/As ratios in pyrite. Ore Geology Reviews, 95, 79–93.

516 Osadchii, E.G., and Gorbaty, Y.E. (2010) Raman spectra and unit cell parameters of
517 sphalerite solid solutions ($Fe_xZn_{1-x}S$). Geochimica et Cosmochimica Acta, 74, 568–
518 573.

519 Pačev ki, A., Libowitzky, E., Zîvkovič, P., Dimitrijevič, R., and Cvetkovič, L. (2008)
520 Copper-bearing pyrite from the Coka Marin polymetallic deposit, Serbia: Mineral
521 inclusions or true solid-solution? The Canadian Mineralogist, 46, 249–261.

522 Palenik, C.S., Utsunomiya, S., Reich, M., Kesler, S.E., Wang, L.M., and Ewing, R.C.
523 (2004) "Invisible" gold revealed: Direct imaging of gold nanoparticles in a
524 Carlin-type deposit. American Mineralogist, 89, 1359–1366.

525 Peterson, D.L., Petrou, A., Giriat, W., Ramdas, A.K., and Rodriguez, S. (1986) Raman
526 scattering from the vibrational modes in $Zn_{1-x}Mn_xTe$. Physical Review B, 33, 1160.

527 Pring, A., Tarantino, S.C., Tenailleau, C., Etschmann, B., Carpenter, M.A., Zhang, M.,
528 Liu, Y., and Withers, R.L. (2008) The crystal chemistry of Fe-bearing sphalerites: an
529 infrared spectroscopic study. American Mineralogist, 93, 591–597.

530 Qian, G.J., Brugger, J., Testemale, D., Skinner, W., and Pring, A. (2013) Formation of
531 As(II)-pyrite during experimental replacement of magnetite under hydrothermal
532 conditions. Geochimica et Cosmochimica Acta, 100, 1–10.

533 Reich, M. and Becker, U. (2006) First-principles calculations of the thermodynamic

534 mixing properties of arsenic incorporation into pyrite and marcasite. Chemical
535 Geology, 225, 278–290.
536 Reich, M., Deditius, A., Chryssoulis, S., Li, J.W., Ma, C.Q., Parada, M.A., Barra, F.,
537 and Mittermayr, F. (2013) Pyrite as a record of hydrothermal fluid evolution in a
538 porphyry copper system: A SIMS/EMPA trace element study. Geochimica et
539 Cosmochimica Acta, 104, 42–62.
540 Reich, M., Kesler, S.E., Utsunomiya, S., Palenik, C.S., Chryssoulis, S.L., and Ewing,
541 R.C. (2005) Solubility of gold in arsenian pyrite. Geochimica et Cosmochimica Acta,
542 69, 2781–2796.
543 Savage, K.S., Tingle, T.N., O'Day, P.A., Waychunas, G.A., and Bird, D.K. (2000)
544 Arsenic speciation in pyrite and secondary weathering phases, Mother Lode gold
545 district, Tuolumne County, California. Applied Geochemistry, 15, 1219–1244.
546 Simon, G., Huang, H., Penner-Hahn, J.E., Kesler, S.E., and Kao, L.S. (1999a)
547 Oxidation state of gold and arsenic in gold-bearing arsenian pyrite. American
548 Mineralogist, 84, 1071–1079.
549 Simon, G., Kesler, S.E., and Chryssoulis, S. (1999b) Geochemistry and textures of
550 gold-bearing arsenian pyrite, Twin Creeks, Nevada: implications for deposition of
551 gold in Carlin-type deposits. Economic Geology, 94, 405–421.
552 Smith, J.E., Brodsky, M.H., Crowder, B.L., Nathan, M.I., and Pinczuk, A. (1971)
553 Raman spectra of amorphous Si and related tetrahedrally bonded semiconductors.
554 Physical Review Letters, 26, 642–646.
555 Sourisseau, C., Cavagnat, R., and Fouassier, M. (1991) The vibrational properties and

556 valence force fields of FeS_2, RuS_2 pyrites and FeS_2 marcasite. Journal of Physics and
557 Chemistry of Solids, 52, 537–544.
558 Spycher N.F. and Reed M.H. (1989) As(III) and Sb(III) sulfide complexes: an
559 evaluation of stoichiometry and stability from existing experimental data. Geochimica
560 et Cosmochimica Acta, 53, 2185–2194.
561 Stingl, T., Müller, B., and Lutz, H.D. (1992) Pyrite-type $RuS_{2-2x}Se_{2x}$ and $Ru_{1-x}Os_xS_2$
562 solid solutions: X-ray structure determination and raman spectra. Journal of alloys and
563 compounds, 184, 275–284.
564 Temple, P.A. and Hathaway, C.E. (1973) Multiphonon Raman spectrum of silicon.
565 Physical Review B, 7, 3685–3697.
566 Twardowski, A., Swagten, H.J.M., Wetering, T., and de Jonge, W.J.M. (1988)
567 Thermodynamic properties of iron-based II–VI semimagnetic semiconductors. Solid
568 state communications, 65, 235–239.
569 Ushioda, S. (1972) Raman scattering from phonons in iron pyrite (FeS_2). Solid state
570 communications, 10, 307–310.
571 Vaughan D. J. and Craig J.R. (1978) Mineral chemistry of metal sulphides Cambridge
572 University Press, Cambridge, London 493p.
573 Vogt, H., Chattopadhyay, T., and Stolz, H.J. (1983) Complete first-order Raman
574 spectra of the pyrite structure compounds FeS_2, MnS_2 and SiP_2. Journal of physics
575 and chemistry of solids, 44, 869–873.
576 Xu, N., Li, S.R., Santosh, M., and Tong, B. (2018) Petrology, geochemistry and zircon
577 U–Pb geochronology of the Jurassic porphyry dykes in the Dehua gold field,

578 Southeast China: genesis and geodynamics. Geological Journal, 53, 547–564.

579 Xu, N., Li, S.R., Wu, C.L., and Santosh, M. (2019) Geochemistry and geochronology
580 of the Dongyang gold deposit in southeast China: Constraints on ore genesis.
581 Geological Journal, 55, 425–438.

582 Yang, M., Huang, D., Hao, P., Zhang, F., Hou, X., and Wang, X. (1994) Study of the
583 Raman peak shift and the linewidth of light-emitting porous silicon. Journal of
584 applied physics, 75, 651–653.

585 Zhang, H, Cai, Y.F., Gang, S., Brugger, J., Pring, A., Ni, P., Qian, G.J., Luo, Z.J.,
586 Zhang., Y., and Tan., W. (2020) Effects of arsenic on the distribution and mode of
587 occurrence of gold during fluid–pyrite interaction: a case study of pyrite from the
588 Qiucun gold deposit, China. Submitted to American Mineralogist.

589 Zhang, H., Cai, Y.F., Zhang, Y., Ni, P., Li, S.N., Ding, J.Y., Pan, Y.G., and Bao, T.
590 (2018) Mineralogical characteristics of silver minerals from the Dongyang Gold
591 deposit, China: Implications for the evolution of epithermal metallogenesis. Journal of
592 Geochemical Exploration, 195, 143–156.

593 Zhu, Q.Q., Cook, N.J., Xie, G.Q., Wade, B.P., and Ciobanu, C.L. (2020)
594 Arsenic-induced downshift of Raman band positions for pyrite. Economic Geology,
595 115, 1589–1600.

596

Figure Captions

Fig. 1. The structure of pyrite represented in terms of FeS_6 octahedra projected along [0 0 1]. Yellow spheres correspond to sulfur ions and red ones to iron ions. The unit cell is indicated by black lines.

Fig. 2. Results of electron microprobe analyses (EMPA) of arsenian pyrite (in at%). (a) Ternary Fe-S-As diagram. The compositions of arsenian pyrites from the Dongyang gold deposit (black circle) (arrow 1) were compared with those from Deditius et al. (2008) (grey triangle) and Zhu et al. (2020) (open circles). The former indicates substitution of As^{1-} for S^{1-} (arrow 1), whereas the Detitius et al. (2008) indicates the substitution of As^{3+} for Fe^{2+} (arrow 2). The compositional trend from Zhu et al. (2020) indicates a mixture of As^{1-} for S^{1-} and As^{3+} for Fe^{2+} substitutions (arrow 3). (b) Diagram showing variations in the concentrations of As^{1-} and S^{1-} within arsenian pyrite for this study and Zhu et al. (2020). (c) Diagram showing variations in the concentrations of As^{3+} and Fe^{2+} within arsenian pyrite for this study and Zhu et al. (2020).

Fig. 3. Backscatter electron (BSE) images showing the As distribution within investigated arsenian pyrite. EMPA positions and associated As concentrations are highlighted in yellow circles and values (in at%). Abbreviations: Py = pyrite.

Fig. 4. Fitting of As^{1-}-pyrite (0.4 at% As and 4.6 at% As) Raman spectrum using the PeakFit program. Goodness of fitting (r^2) > 0.998.

Fig. 5. Representative room-temperature Raman spectra of natural As^{1-}-pyrites between 250 and 500 cm^{-1}. Composition expressed as at% As in FeS_2.

619 **Fig. 6.** Variation in wavenumber and FWHM of Raman bands as a function of atomic
620 fraction of arsenic in pyrite. A linear baseline was subtracted from all the spectra.

621 **Fig. 7.** (a) Variation in intensity ratios of the A_g band relative to the E_g band as a
622 function of atomic fraction of arsenic in pyrite. (b-d) Comparison of wavenumber and
623 intensity of Raman bands for pyrite grains with different crystal orientations and As
624 contents. Crystal orientation expressed as Euler angles. The intensity ratio of A_g
625 relative to E_g is calculated for each spectrum.

626

627

628

This is the peer-reviewed, final accepted version for American Mineralogist, published by the Mineralogical Society of America.
The published version is subject to change. Cite as Authors (Year) Title. American Mineralogist, in press.
DOI: https://doi.org/10.2138/am-2021-7806. http://www.minsocam.org/

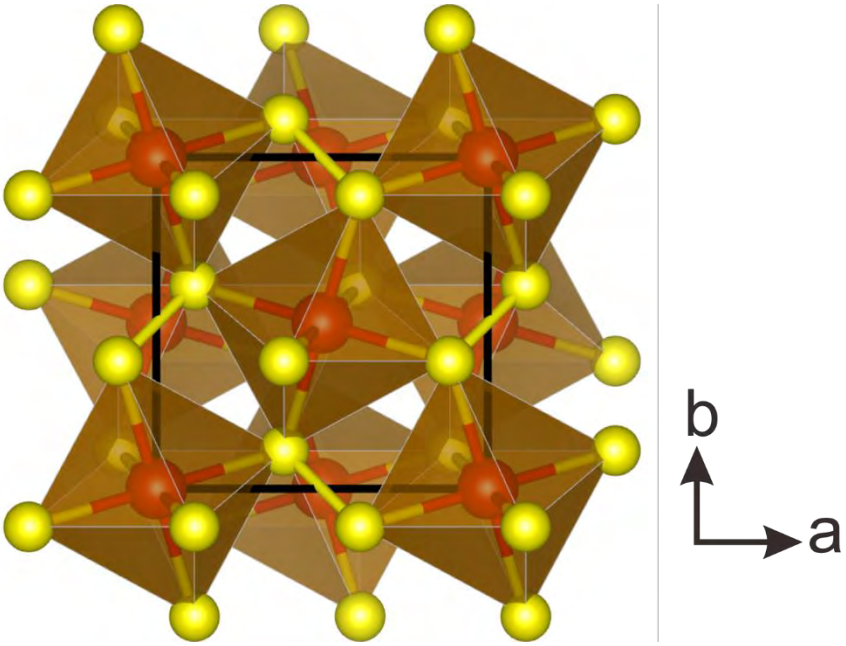

629

630 Figure 1

631

632

This is the peer-reviewed, final accepted version for American Mineralogist, published by the Mineralogical Society of America.
The published version is subject to change. Cite as Authors (Year) Title. American Mineralogist, in press.
DOI: https://doi.org/10.2138/am-2021-7806. http://www.minsocam.org/

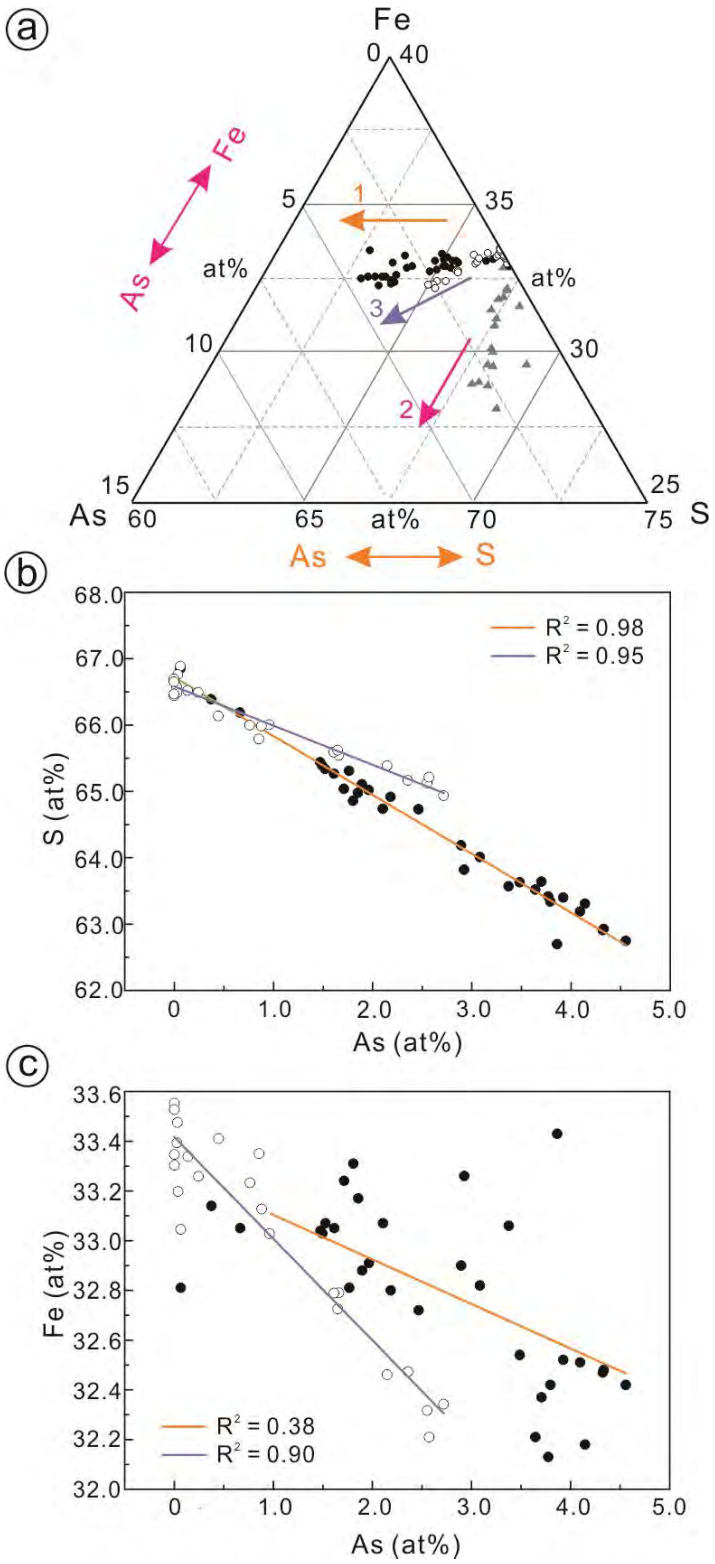

633

634 Figure 2

635

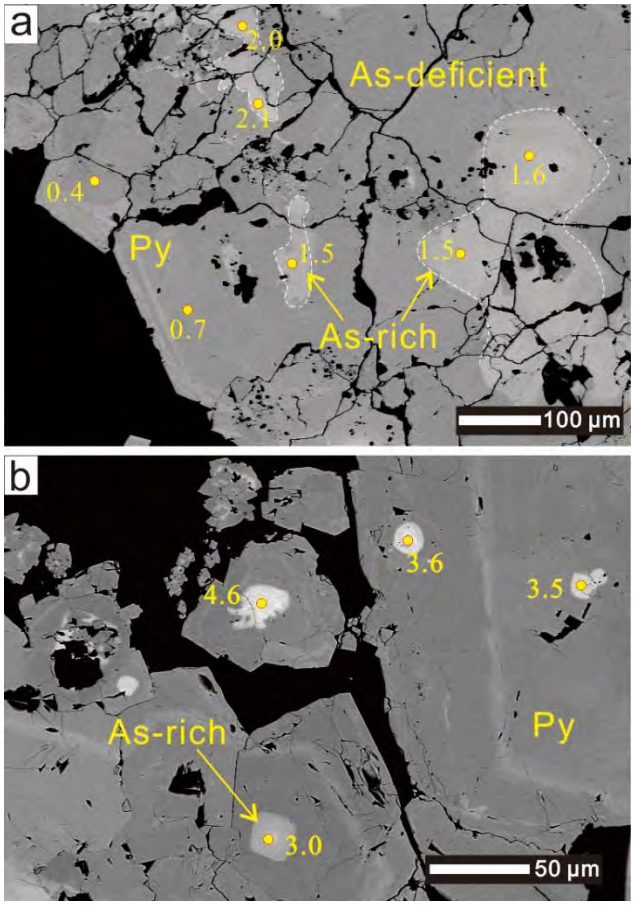

Figure 3

This is the peer-reviewed, final accepted version for American Mineralogist, published by the Mineralogical Society of America.
The published version is subject to change. Cite as Authors (Year) Title. American Mineralogist, in press.
DOI: https://doi.org/10.2138/am-2021-7806. http://www.minsocam.org/

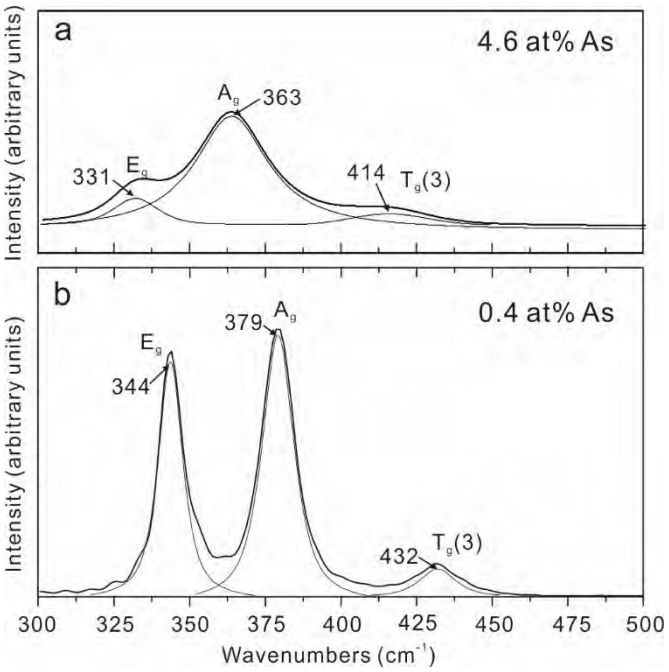

639

640 Figure 4

641

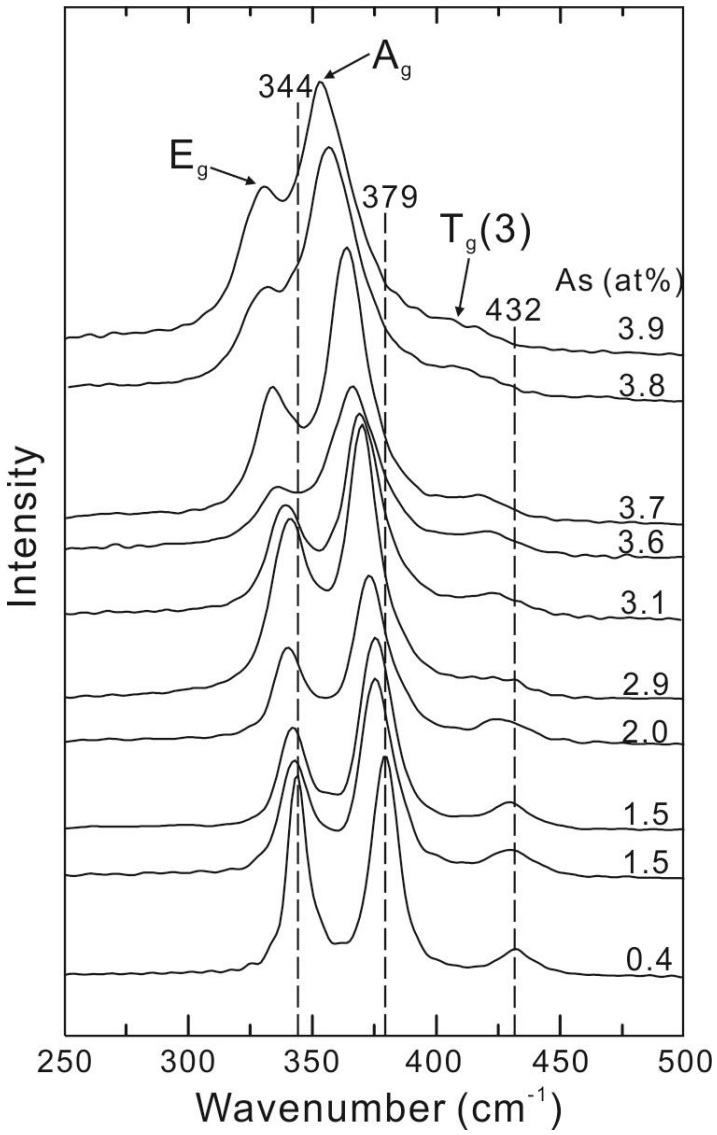

Figure 5

This is the peer-reviewed, final accepted version for American Mineralogist, published by the Mineralogical Society of America.
The published version is subject to change. Cite as Authors (Year) Title. American Mineralogist, in press.
DOI: https://doi.org/10.2138/am-2021-7806. http://www.minsocam.org/

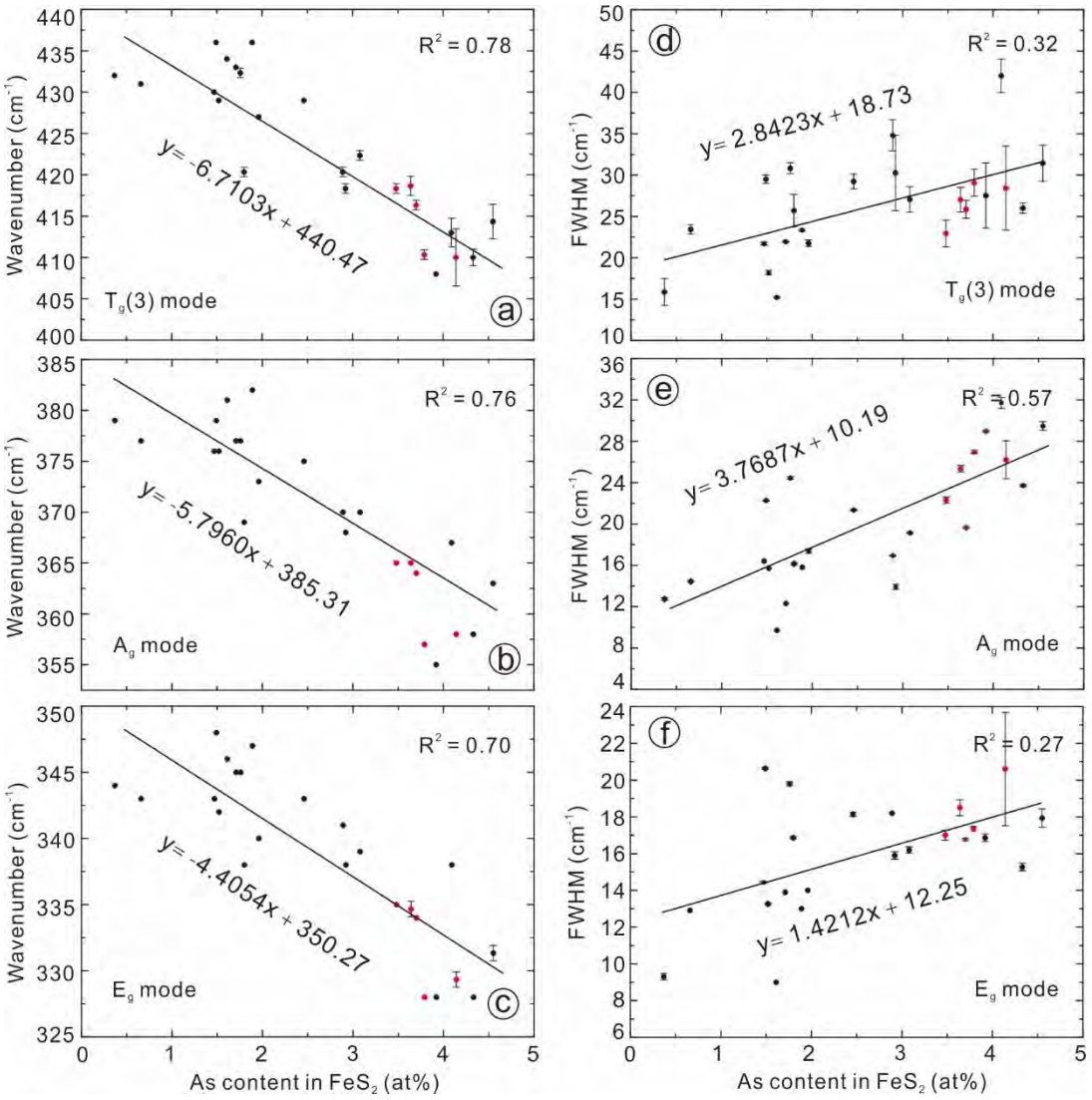

Figure 6

This is the peer-reviewed, final accepted version for American Mineralogist, published by the Mineralogical Society of America.
The published version is subject to change. Cite as Authors (Year) Title. American Mineralogist, in press.
DOI: https://doi.org/10.2138/am-2021-7806. http://www.minsocam.org/

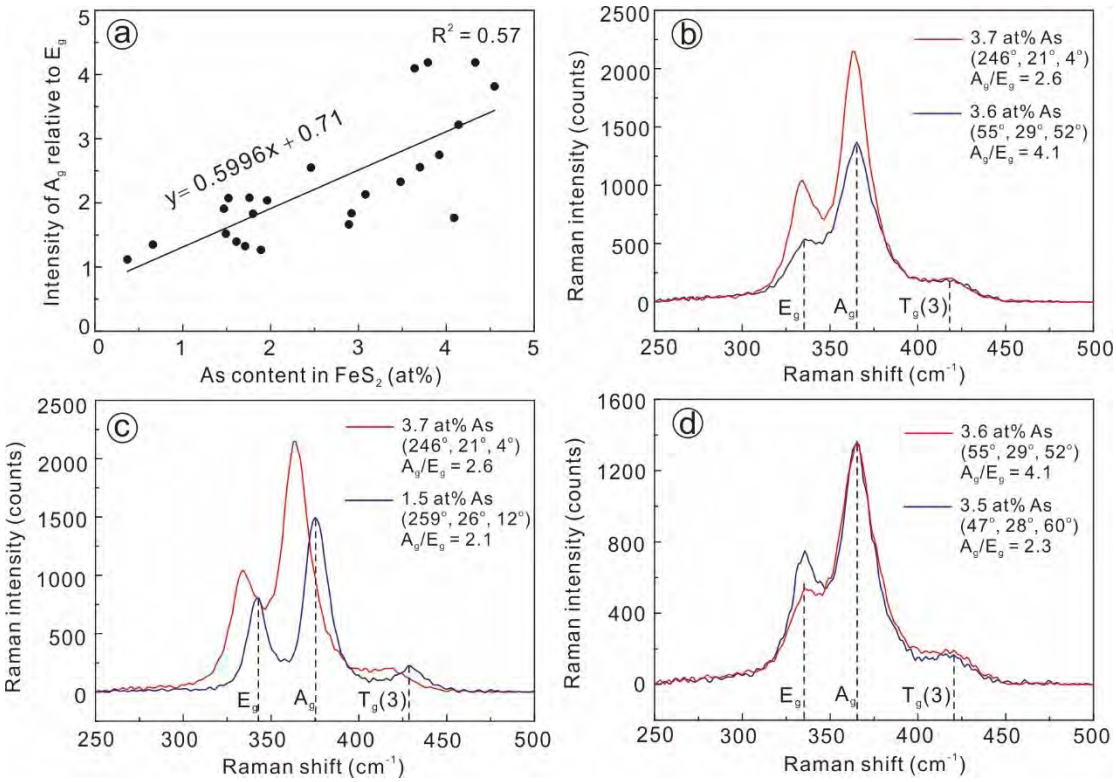

649

650 Figure 7